Localisation of normal faults in multilayer sequences

Martin P.J. Schöpfer *, Conrad Childs, John J. Walsh

Fault Analysis Group, School of Geological Sciences, University College Dublin, Belfield, Dublin 4, Ireland

Abstract

Existing conceptual growth models for faults in layered sequences suggest that faults first localise in strong, and brittle, layers and are later linked in weak, and ductile, layers. We use the discrete element method for modelling the growth of a normal fault in a brittle/ductile multilayer sequence. The modelling reveals that faults in brittle/ductile sequences at low confining pressure and high strength contrast localise first as Mode I fractures in the brittle layers. Low amplitude monoclinal folding prior to failure is accommodated by ductile flow in the weak layers. The initially vertically segmented fault arrays are later linked via shallow dipping faults in the weak layers. Faults localise, therefore, as geometrically and kinematically coherent arrays of fault segments in which abandoned fault tips or splays are a product of the strain localisation process and do not necessarily indicate linkage of initially isolated faults. The modelling suggests that fault tip lines in layered sequences are more advanced in the strong layers compared with weak layers, where the difference in propagation distance is most likely related to strength and/or ductility contrast. Layer dependent variations in fault localisation rates generate fringed rather than smooth fault tip lines in multilayers.
© 2006 Elsevier Ltd. All rights reserved.

Keywords: Discrete element method; Fault growth; Fault refraction; Fault tip line; Mohr circles; Stress and strain paths

1. Introduction

There are a variety of conceptual models for the growth of faults in mechanically layered (brittle/ductile) sequences, all of which acknowledge that faults commonly show lithologically controlled dip changes on cross-sections, with steeper fault dips in strong layers and shallower dips in weaker layers (Fig. 1). These dip changes are attributed to a variety of mechanisms (Ferrill and Morris, 2003 and references therein): (i) post-faulting differential compaction, (ii) active faulting, with slip along layers or intersecting faults, (iii) linkage of an originally vertically-segmented fault, and (iv) fault initiation and propagation with dip controlled by rock properties and effective stresses. Two of these mechanisms ((iii) and (iv)), which are not mutually exclusive, underpin the most popular models for the growth of faults within layered sequences. For mechanism (iii) faults first localise in the strong layers and are later linked via faults in the weak layers (Eisenstadt and De Paor, 1987; Peacock and Sanderson, 1992; McGrath and Davison, 1995; Childs et al., 1996; Crider and Peacock, 2004). In this case, fault localisation and dips within the strong layers

are controlled by rock properties and deformation conditions, and therefore by the failure mode and/or failure angles, while dips within the weak layers are a consequence of segment linkage. An alternative model (iv) suggests that localisation and associated dip changes do not develop in association with fault segmentation and are entirely controlled by the failure mode and failure angles of the faulted weak and strong layers. Distinguishing between these models on observational or theoretical grounds is not, however, always straightforward.

Ferrill and Morris (2003) describe small-scale faults exhibiting lithologically controlled dip variations (Fig. 2a) They consider two mechanisms of formation for the fault geometries they observe, with either fault localisation first occurring within the strong layers (Fig. 2b) or fault localisation first occurring within the weak layers (Fig. 2c). In both cases fault dips are determined by the rheological properties of the layers with steep dips in the strong layers and relatively shallow dips in the weak layers. The faults studied by Ferrill and Morris (2003) do not have geometrical features that might indicate whether they initiated in the strong or weak layers, e.g. abandoned tips or splays. Other workers have described faults with lithologically controlled dip variations that, from field relations, can be demonstrated to have formed by linkage of segments that formed within the strong layers (e.g. Peacock and Zhang, 1993; Childs et al., 1996). The absence of discriminating traits of segmentation may support

---

* Corresponding author. Tel.: +353 1 7162611; fax: +353 1 7162607.
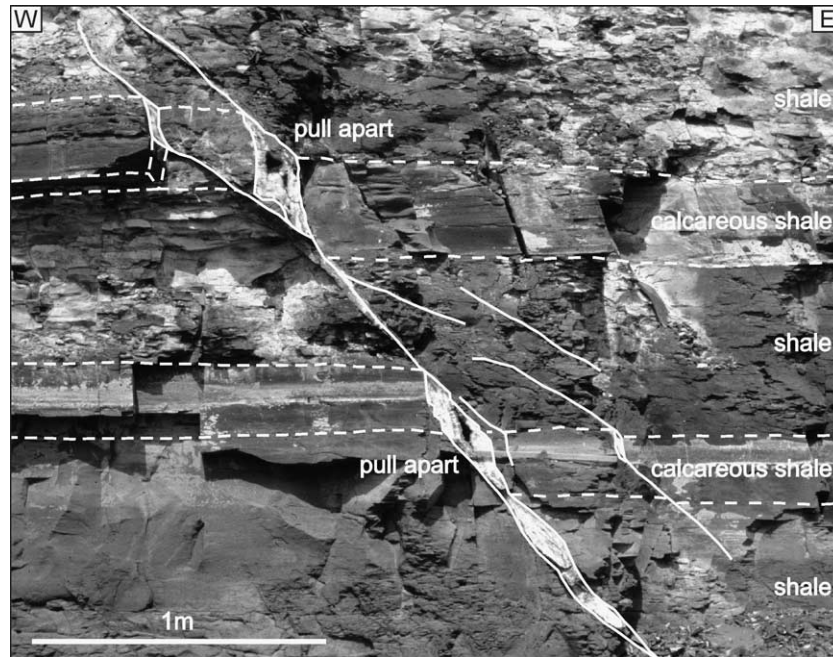*E-mail address:* martin@fag.ucd.ie (M.P.J. Schöpfer).

Fig. 1. A small-scale normal fault (displacement = 30 cm; downthrows to the right) exposed in a cliff-section east of Kimmeridge Bay, Dorset, UK, which illustrates the importance of lithological control on fault dip and fault refraction. This normal fault cuts a shale-dominated sequence (Kimmeridge Clay Formation, Upper Jurassic) that contains calcareous shale layers. Within these calcareous shales, fault segments are nearly vertical and are linked via shallow dipping faults within the weaker shale layers. Fault displacement on this 'staircase' geometry leads to the development of pull-aparts.

the application of a model in which the faults were not, in fact, segmented in their early stages of growth, but formed by refraction across bedding planes during progressive forward tip-line propagation (Fig. 2d).

Although both linkage and forward propagation models (Fig. 2) provide a plausible rationale for field observations that can be related to failure criteria, they otherwise lack a mechanical basis. Mechanical analyses using failure criteria (e.g. Coulomb–Mohr, Griffith) can provide useful insights into

the orientation of principal stresses and consequently faults, but do not allow definition of the relative timing of failure and localisation in a mechanical multilayer (Mandl, 2000).

Since observational data and theoretical grounds do not provide a definitive answer to questions relating to the localisation of faults within multilayers, we use a numerical approach that is capable of modelling the localisation of faults within multilayer sequences. The aim of this paper is to provide a mechanical basis for the localisation and linkage of normal
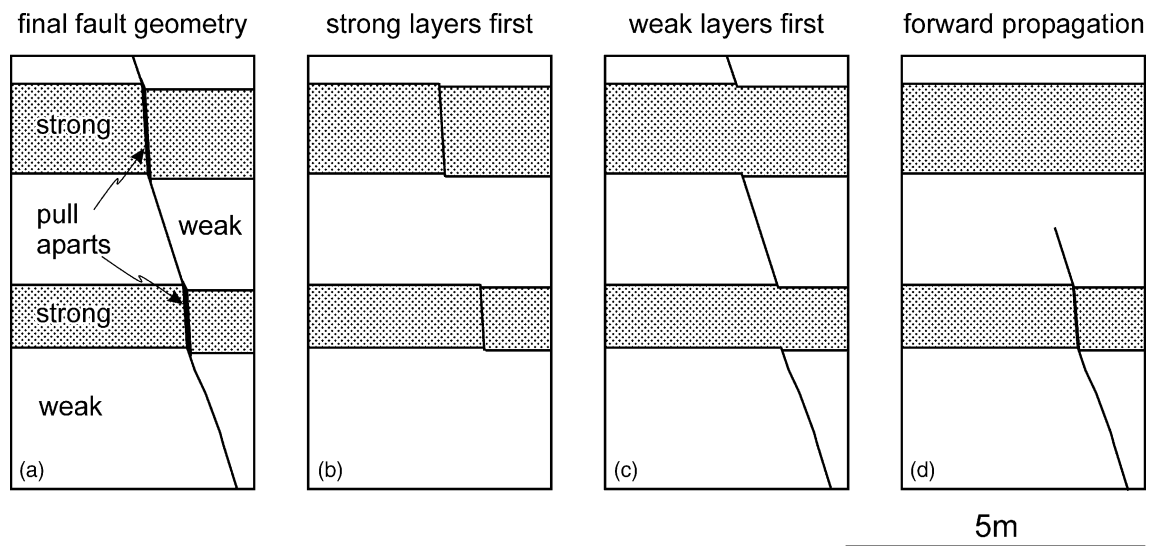

Fig. 2. (a) Schematic geometry of normal faults cutting limestone layers of the Cretaceous Buda Limestone exposed along Interstate Highway 10 (I-10), in west Texas and three possible models for their growth ((b)–(d)) (after Ferrill and Morris, 2003, their table 1 and fig. 5). In (b) the faults localise first in the strong layers and the steep segments are later linked via shallow faults. In (c) the faults localise first in the weak layers and the shallow segments become linked via steep faults. In (d) the fault trace is not initially segmented but the trajectory of the upward propagating fault tip changes as it crosses a lithological interface, i.e. a bedding plane.

faults in a layered sequence using the discrete element method (DEM). The DEM has recently been used for modelling the formation of accretionary wedges (Burbidge and Braun, 2002), fault-propagation folds (Finch et al., 2003, 2004), out-of-plane fault propagation (Strayer and Suppe, 2002) and the interaction of two overlapping faults (Imber et al., 2004). The method is capable of modelling failure and localisation without the necessity to define constitutive equations, as is the case for the more commonly used continuum methods. It is therefore the ideal tool for addressing questions relating to fault localisation in multilayered brittle/ductile sequences. As is described later, our models comprise brittle materials that deform by elastic deformation followed by fracturing and ultimately failure at peak strength, whilst our ductile material is frictional-plastic throughout deformation, displaying an inelastic deformation response without fracturing; these materials lead to macroscopic deformations that are discontinuous and continuous, respectively. The results of the modelling support the notion that vertically segmented fault arrays initially develop in the strong, and brittle, layers and are later linked by shallower dipping faults in the weak, and ductile, layers.

2. Methods

2.1. Principles of DEM

The DEM is a broad class of methods for modelling the finite displacements and rotations of discrete bodies (Cundall and Hart, 1992). The DEM can be implemented in two and three dimensions. We use a 2D approach with circular particles as introduced by Cundall and Strack (1979) and implemented in commercially available software (PFC-2D; Itasca Consulting Group, 1999). Particles are treated as rigid discs and are allowed to overlap at particle–particle and particle–wall contacts. Walls are rigid boundaries of arbitrary shape, to which constant velocity or constant stress conditions can be applied. The amount of overlap at each contact is small compared with particle size and the contact normal force is linearly related to the amount of overlap. If the contact shear force exceeds a critical value, which is determined by a contact friction coefficient, slip occurs at the contact. Particles can be bonded together with linear elastic cement (parallel bond model; Itasca Consulting Group, 1999; Potyondy and Cundall, 2004) and if the critical tensile or shear stress (which is typically normally distributed in a bonded model) at a bonded contact is exceeded the bond breaks.

For a more detailed description of this numerical method the reader is referred to Cundall and Hart (1992), Hazzard et al. (2000), Potyondy and Cundall (2004) and references therein.

2.2. Model material calibration

In contrast to continuum methods, where the rheology of the model material is defined using constitutive laws, the macroscopic response of the (bonded) particle assemblage in DEM models has to be calibrated using a numerical laboratory. The microproperties (particle size and size distribution, particle

and bond stiffness, contact friction, bond strength) are adjusted, mainly by trial and error, to obtain the desired model macroscopic response calibrated to laboratory rock deformation data. The resulting microproperties do not replicate true grain-scale physics because the model particles are orders of magnitude larger than the grains of the equivalent rock and each particle therefore represents a small volume of rock. Although our approach did not attempt to exactly reproduce the rheology of a particular rock based on experimental data, the macroscopic properties of our model materials reproduce the general rheological behaviour of a strong, brittle material and a weak, ductile one.

The particles in this study have a uniform size distribution with radii ranging between 31.25 and 62.50 mm, respectively. The rheology of a strong material, consisting of bonded particles, and a weak material, consisting of non-bonded particles, was investigated. The bonded particles have normal and shear contact/bond stiffnesses of 50 and 16.7 GPa, respectively, a contact friction coefficient of 1.0 and normally distributed tensile and shear bond strengths with means of 250 and 125 MPa and coefficients of variation of 1/12 and 1/6, respectively. The bond strength distributions have cut-offs of ± 2 standard deviations and the width of each bond is half the radius of the smaller of the two bonded particles. The non-bonded particles have the same particle sizes and therefore size distribution, as the bonded material, a normal and shear contact stiffness of 50 GPa and 16.7 GPa, respectively, and a contact friction coefficient of 0.5.

The strength of bonded materials is sample size dependent (strength decreases with increasing sample size; Potyondy and Cundall, 2004), thus proper calibration requires tests on samples at a scale appropriate to the model. In our multilayer model, the basic mechanical unit is one bed. Therefore the rheology of both the bonded and non-bonded material was investigated using calibration sample widths equal to the thickness of the strong layers in the multilayer, i.e. 1 m (see below).

The rheology of the non-bonded material was investigated using confined (25 MPa) biaxial compression tests on samples that are 1 m wide and 2 m high. Since the material is cohesionless and exhibits no (bulk) elasticity, the only bulk property that was calculated for each test ($N = 30$) is the friction coefficient, which can be easily obtained for straight failure envelopes.

The rheology of the bonded material was investigated using unconfined biaxial compression tests on samples that are 1 m wide and 2 m high. These tests ($N = 30$) were used for calculating the bulk elastic properties (Young's modulus, Poisson's ratio) and provided the unconfined compressive strength. Additionally, direct tension tests on dog-bone shaped samples ($N = 196$) with a central thickness of 1 m were performed at various confining pressures in order to define the failure envelope in the tensile stress field.

Although calibration tests on 1 m wide samples provide the bulk rheological properties and their variability at the scale of the multilayer model, they do not give insights into strain distribution (e.g. localisation) within the sample due to their poor resolution (ca. 10 particles wide). To examine localisation
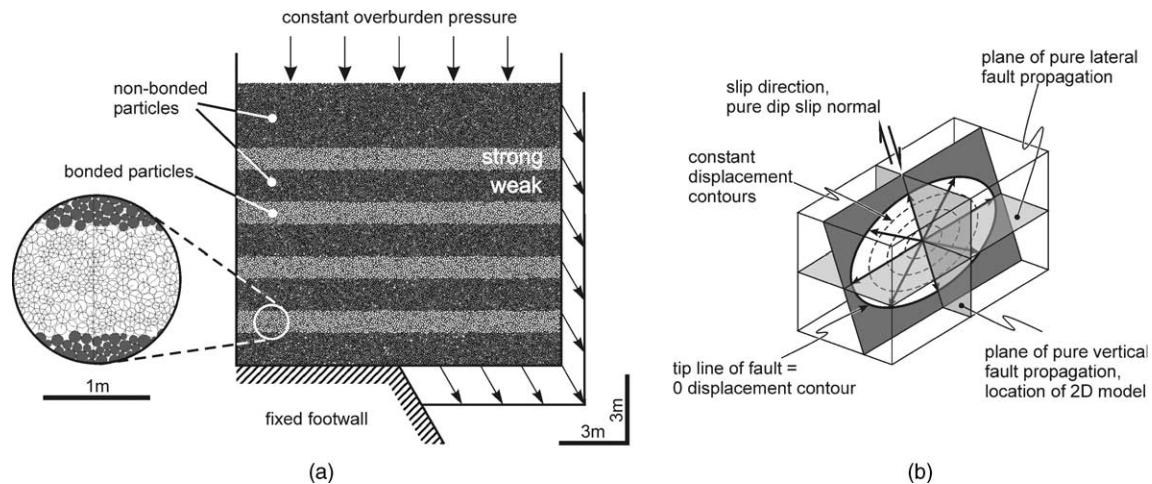
Fig. 3. Model boundary conditions. (a) PFC-2D model consisting of >23,400 cylindrical particles. The strong and weak layers consist of bonded and non-bonded particles, respectively (bonds are shown in enlarged figure). Overburden pressure is approximately 23 MPa and the hanging wall moves with constant velocity parallel to a predefined fault at the base of the model. (b) Schematic block diagram showing the propagation directions of an ideal elliptical normal fault. The tip line bounds an elliptical area of failed rock (white). Since the fault plane propagates radially (arrows show tip line propagation direction) only two sections (shaded) have no out-of-plane fault propagation. The 2D numerical model is located within the plane of no lateral fault propagation. This fault is shown schematically as a single fault surface, but in all probability will comprise an array of segments.

behaviour in our model materials nine biaxial tests were performed on samples that are 5 m wide and 10 m high and contain over 6000 particles.

2.3. Multilayer faulting model boundary conditions

The multilayer model used is 15 m wide, 13 m high and is comprised of >23,400 particles (Fig. 3a). The model is composed of four 1 m thick strong (bonded particles) and four 1.5 m thick weak (non-bonded particles) layers. The top 3 m of the model comprises a layer of non-bonded particles. The primary function of this top layer is model confinement, which is achieved by applying a force equivalent to a lithostatic stress of approximately 23 MPa (ca. 1 km burial depth) to particles at the surface of the model. The sides and base of the model are defined by two rigid L-shaped walls which meet at a predefined 60° dipping fault at the base of the model. The L-shaped hanging wall is moved with constant velocity parallel to the predefined fault; this pre-conditioning ensures the formation of one fault, rather than several faults. The model is saved in 1 cm throw increments and the final throw is 10 cm; models with throws beyond the point of localisation (ca. 10 cm) will be published elsewhere. With respect to the ideal elliptical fault surface shown in Fig. 3b, the model is located in the plane of no lateral propagation along a chord through the point of maximum displacement.

2.4. Stress and strain in discontinua

Stress and strain are continuum concepts, whereas our model material is comprised of discrete particles and is therefore a discontinuum (compressive stress positive and $\sigma_I > \sigma_{II} > \sigma_{III}$). Various methods for homogenising DEM models to allow comparison with continuum mechanics solutions have

been proposed and successfully implemented (e.g. O'Sullivan et al., 2003). The stress tensor can be obtained for each particle in our models, but the state of stress at this point is meaningless on a macroscale, i.e. on the scale of the layers. To homogenise particle stresses the average stress tensor is calculated for circular regions (Potyondy and Cundall, 2004).

The deformation tensor **D**, which is sometimes called the positions gradient tensor (see Appendix A), can be obtained for small and large strains using the least-squares method described in Oda and Iwashita (2000). For each circular region (diameter depends on the scale of interest) the particle closest to the centre is found and the relative displacements of particles surrounding this particle are calculated in order to remove the translational component of deformation. Once this translation has been removed the best-fit displacement gradient tensor can be calculated, enabling the deformation tensor **D** and the Lagrangian strain tensor **E** to be obtained.

For the maximum shear strain contour diagrams shown (e.g. Figs. 4e and f and 6), the displacement gradient tensor is obtained for each particle for a circular, 0.3 m diameter, homogenisation area containing, on average, eight particles. Since the averaging region is a small proportion of the model dimensions, contours of maximum shear strain are typically quite irregular. We present both finite and incremental strain contours to illustrate fault evolution. Incremental strains are calculated in 1 cm throw intervals, where for each particle the accumulated displacement of the previous stage is subtracted. The best-fit deformation tensor for each 1 cm throw increment can then be obtained for each particle using the same method described above.

For the definition of the stress and strain paths at selected locations within our model (Fig. 8) we use 1 m diameter homogenisation areas, containing on average 92 particles, to minimize noise. Strain paths are represented using Mohr circles
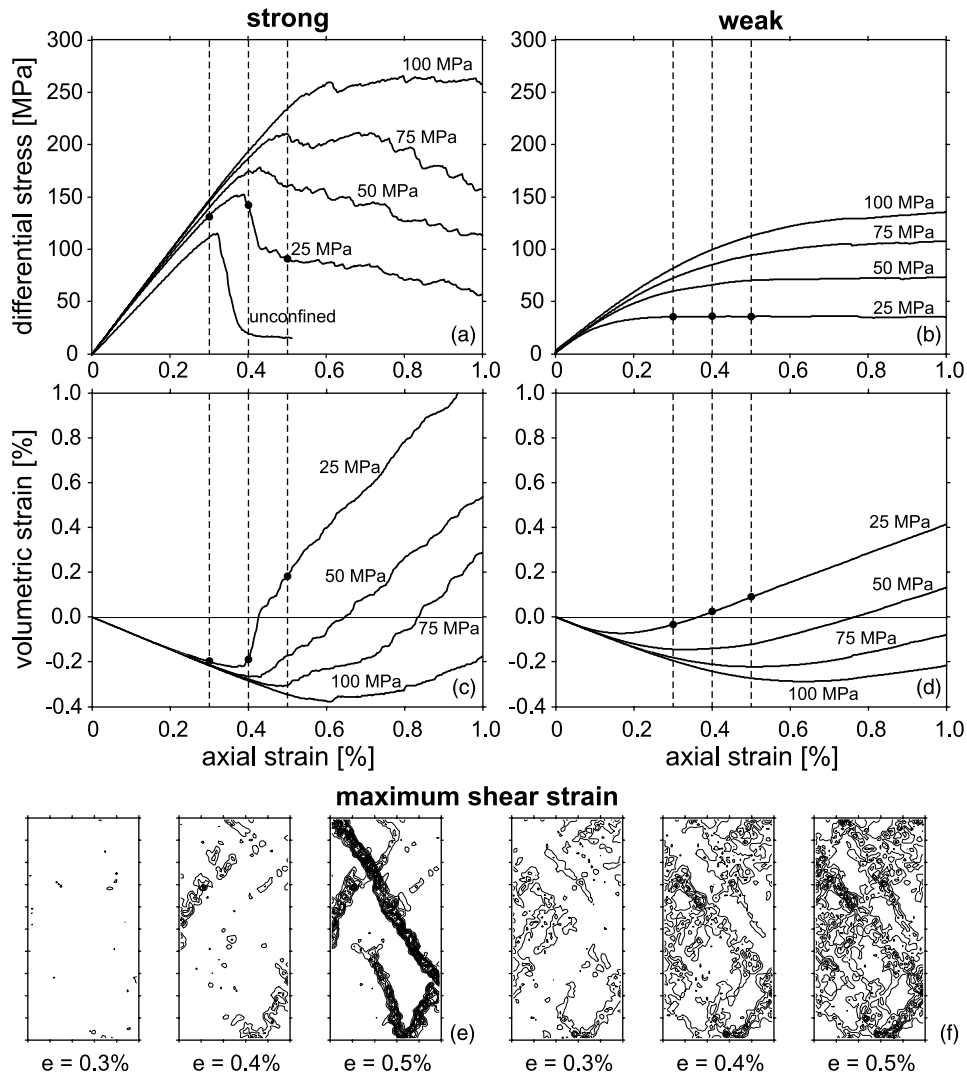
Fig. 4. (a)–(d) Plots illustrating the results of rheological testing of the strong ((a) and (c)) and weak ((b) and (d)) materials comprising the multilayer models at various confining pressures (labelled curves). Vertical dashed lines are drawn at 0.3, 0.4 and 0.5% axial strain. (e) and (f) Contour plots showing the distribution of maximum finite shear strain (contour interval is 0.005) within models comprising the strong (e) and weak (f) materials at axial strains of 0.3, 0.4 and 0.5% and a confining pressure of 25 MPa. All data are for high resolution 5 m wide and 10 m high models.

for the deformation tensor, which are briefly reviewed in Appendix A.

3. Results

3.1. Macroproperties of model material

Stress vs. axial strain and volumetric strain (strictly speaking area change in a 2D model) vs. axial strain curves for the strong and weak model material are shown in Fig. 4. Additionally, maximum shear strain contour plots for selected biaxial test samples are shown (Fig. 4e and f) in order to illustrate strain localisation. The strong material exhibits elasticity and compaction prior to failure (Fig. 4a). The axial strain at failure and the differential stress at failure increase with increasing confining pressure (Fig. 4a). The amount of strain softening decreases with increasing confining pressure, i.e. the material becomes more ductile. The weak material

exhibits steady-state flow after a non-linear increase in differential stress (Fig. 4b). The steady-state stress increases with increasing confining pressure. The lack of strain softening in the weak material is probably due to the use of rigid platens as lateral boundaries, which do not allow the formation of a single through-going shear zone (O'Sullivan, pers. comm., 2004). A comparison of the volumetric strain curves for the strong and weak material (Fig. 4c and d) reveals that at low confining pressures (e.g. 25 MPa, see also maximum shear strain contour plots, Fig. 4e and f) the weak material dilates and localises earlier than the strong material. However, from these figures it is clear that the strong material localises strain better because it exhibits greater strain softening.

Young's modulus and Poisson's ratio (assuming plane strain; Potyondy and Cundall, 2004) were obtained for the unconfined biaxial tests (sample width 1 m, $N = 30$) and determined at half the axial strain to failure and are 21.8 ± 1.6 GPa and 0.29 ± 0.06, respectively. Principal stress

diagrams with best-fit failure envelopes are shown in Fig. 5. For the strong material a Coulomb–Mohr criterion with tension cut-off (Paul, 1961) was fitted to the results of direct tension tests on dog-bone shaped samples. The best-fit parameters with curves representing the associated probability distributions are plotted in Fig. 5 and reveal that the unconfined compressive strength, cohesion and friction coefficient are typical of those for strong sedimentary rocks (e.g. Hoek and Brown, 1997; Tsiambaos and Sabatakakis, 2004). However, the ratio of unconfined compressive strength to tensile strength is low (3.5) compared with natural rocks (e.g. 9–17; table 6.15.1 in Jaeger and Cook, 1976). These low ratios are typical for DEM models using smooth, circular particles (Fakhimi, 2004) and can be improved by using either irregular shaped particles (clumps), by introducing a bending resistance between chains of bonded particles (Cundall, pers. comm., 2004) or by increasing sample resolution (table 3 in Potyondy and Cundall, 2004). For the purpose of this article in which we examine fault localisation within a brittle/ductile sequence, absolute strength values are however subordinate, with strength contrast and rheology the main controlling factors. For the non-bonded material the average friction coefficient was calculated from the confined
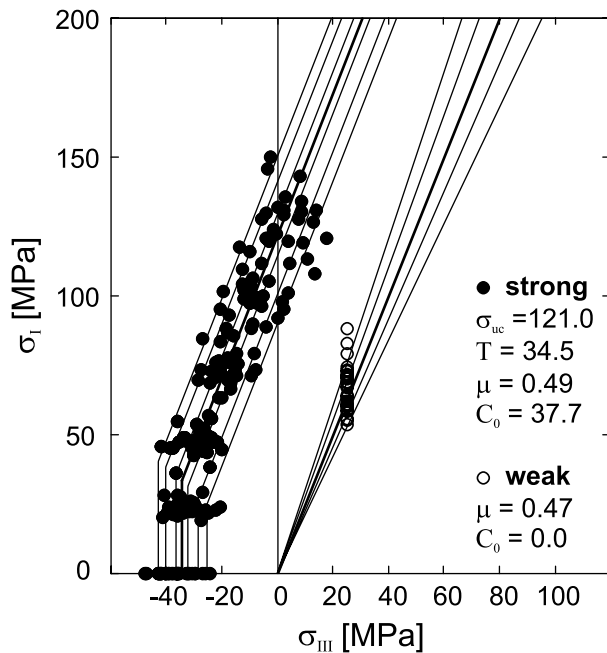

Fig. 5. Principal stress diagram with best-fit failure envelopes (bold lines) for the strong and weak material. The data for the strong material were obtained from direct tension tests on dog-bone shaped samples with a central width of 1 m at various confining pressures and each data point represents the state of stress at failure ($N=196$). The data for the weak material were obtained from confined (25 MPa) biaxial compression tests and each data point represents the peak stress during loading ($N=30$). The best-fit macroproperties are given, where $\sigma_{uc}=$unconfined compressive strength (MPa), $T=$tensile strength (MPa), $C_0=$cohesion (MPa) and $\mu=$friction coefficient. For the strong material the different curves represent the 0.01, 0.5, 0.25, 0.50, 0.75, 0.95 and 0.99 percentile of the probability distribution. For the weak material the average friction coefficient and the average ±1 and ±2 standard deviations are shown.

biaxial tests as 0.47 ± 0.05 (standard deviation). The Coulomb–Mohr criterion is plotted using the average friction coefficient and no cohesion (Fig. 5).

In summary, material properties and rheology of the strong layers are comparable with those of strong sedimentary rocks (e.g. Hoek and Brown, 1997; Tsiambaos and Sabatakakis, 2004), whilst the weak layers have no tensile strength and are comparable with some shales (e.g. Petley, 1999).

3.2. Fault growth and geometry in a multilayer sequence

Fig. 6 shows the propagation of a fault through a multilayer model at throw (*t*) increments of 1 cm. The stages of fault evolution are illustrated with contours of incremental maximum shear strain for each stage. Although the total 10 cm offset is not visible from the layer interfaces, fault development can be examined from the changing pattern of low incremental strains. Fig. 6 is complemented by the profiles of strain and rotation for layer E at 2 cm throw increments (Fig. 7), which were obtained using 1-m-wide circular homogenisation regions with a spacing of 10 cm.

At low displacements (<3 cm) diffuse zones of deformation develop on either side of the lowest strong layer (G; Fig. 6). Up to throws of 3 cm, formation of a low-amplitude precursory fold within this strong layer is accommodated by flow in the underlying and overlying weak layers. At a throw of 4 cm, the lowest strong layer (G) fails in tension (Mode I fracture) and subsequent strain is concentrated on this fault. At throws of 5–7 cm, flow in the weak layers accommodates folding of the second strong layer (E) until it fails in tension arising from outer-arc extension associated with monoclinal folding; folding is highlighted by the plateaux of other curves shown in Fig. 7b. Flow in the weak layers is principally accommodated within diffuse zones that are located in the hanging wall of the incipient fault and have an overall antithetic shear sense (see below). These antithetic shear zones intersect the tops of the strong layers at the point of greatest outer arc extension associated with monoclinal folding. At a throw of 8 cm two additional Mode I fractures have formed, one in the topmost layer (A), collinear with the array of underlying Mode I fractures, and another one in the hanging wall of the lowest layer (G). The latter is located on the hanging wall hinge of the monoclinal flexure of the lowermost strong layer and propagates from bottom to top, a direction that is again consistent with outer arc extension. At this stage one of the strong layers (C) is still intact, even though it is overlain and underlain by strong layers containing an approximately collinear array of Mode I fractures, demonstrating that the failure of layers within a multilayer does not necessarily occur in forward sequence. At a throw of 9 cm the fault has cut through all of the strong layers within the sequence and although it begins to localise within the weak layers, it has yet to do so in the central weak layer (D). This anomaly arises due to the localisation of a second Mode I fracture in the second lowest strong layer (E). This new fracture formed in the hanging wall side of the earlier fracture, which became inactive over the 8–9 cm interval but became active again between
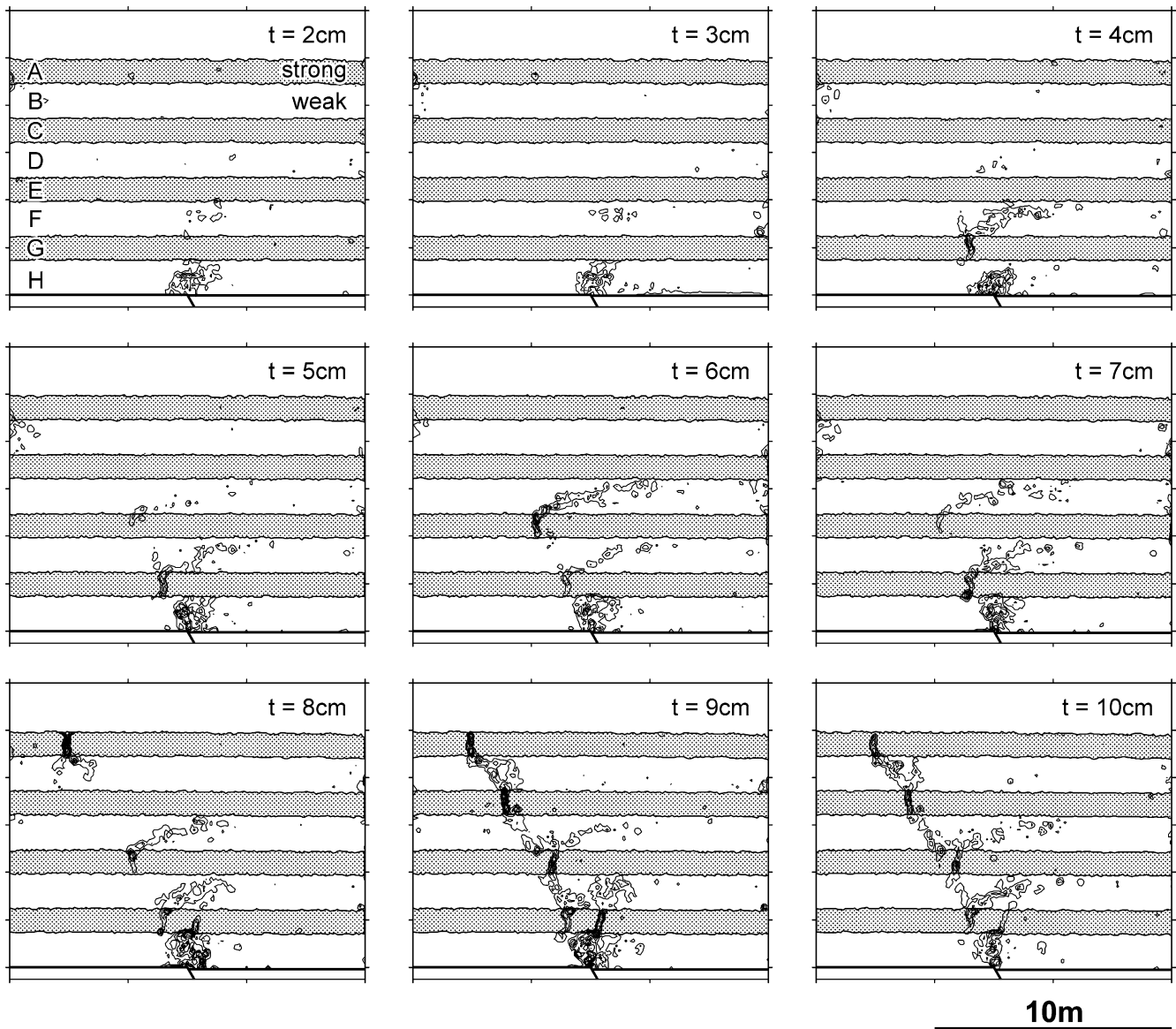
Fig. 6. Incremental maximum shear strain contour plots (contour interval is 0.005) of PFC-2D model of normal fault growth in a brittle/ductile sequence (*t*=throw). The different layers within the model are labelled A–H (See upper left-hand plot). See text for further explanation.

9 and 10 cm throw. At 10 cm throw a continuous, through-going fault is established. This fault has a 'staircase' geometry in which vertical faults within the strong layers are linked by approximately 50° dipping faults in the weak layers, producing an average dip of ca. 60°. Although individual fault segments first develop within strong layers and do not progress simply from bottom to top of the model, the final geometry is relatively simple and coherent. This coherence suggests that the deformation of both strong and weak layers throughout the model is strongly coupled, details of which are investigated below.

3.3. Stress and strain paths

The centre diagram in Fig. 8 shows the model in Fig. 6 at the final throw of 10 cm contoured for maximum finite shear strain (contour interval is 0.01). Strain and stress paths were

determined at 12 selected locations (Fig. 8). In each circular region of 1 m diameter the average stress tensor and displacement gradient tensor were obtained at 1 cm throw intervals. For the strong layers, six locations of Mode I fracturing were analysed, four along the eventual through-going fault and two hanging wall splays. In the weak layers, four regions were examined between the main Mode I fractures in the strong layers and along the eventual through-going fault and two regions were selected within the low-angle antithetic shear zones in the hanging wall of the eventual through-going fault. The strain paths are shown in Fig. 8 using Mohr circles for the deformation tensor (see Appendix A for a brief review). Rotations and stretches are easily read off these diagrams (see Fig. A2 for ideal deformation paths) and large volumetric strains can be simply calculated by the product of the principal stretches. However, the volumetric strains and rotational components of strain in this model were initially small
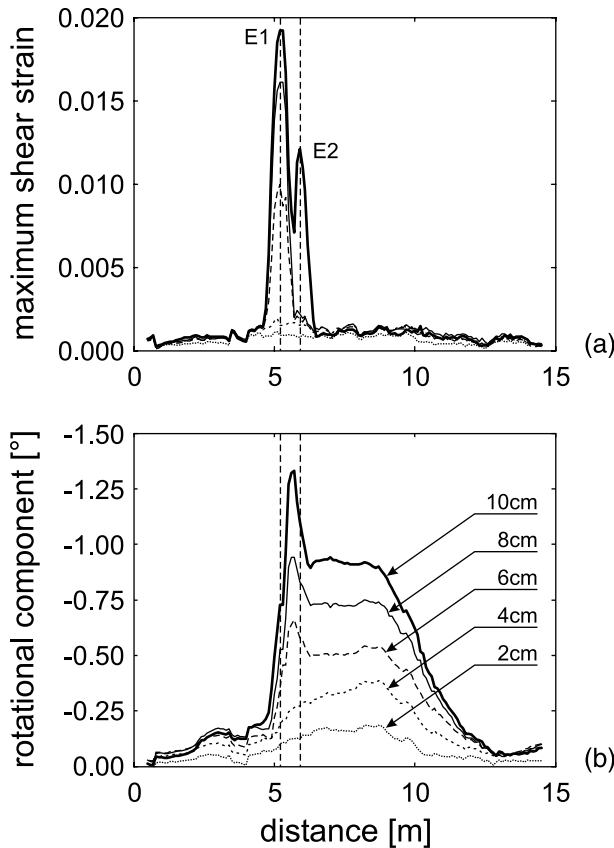
Fig. 7. Strain profiles in 2 cm throw increments (labelled in (b)) along the centre of layer E of Fig. 6. The maximum finite shear strain (a) and the rotational component of deformation (b) were obtained for 1-m-wide circular homogenisation regions with 10 cm spacing. The two vertical dashed lines are the locations of Mode I fractures (labelled E1 and E2; see Figs. 6 and 8). The plateaux of the curves in (b) correspond to the limb of the monocline, the left hand hinge of which fails between 5 and 6 cm throw.

and are therefore shown separately in Fig. 9 for each locality. Stress paths are shown in principal stress diagrams in Fig. 10, in which the experimentally derived failure envelopes for the strong and weak materials (Fig. 5) are plotted.

The strain and stress paths of the 12 locations identified in Fig. 8 are described in four groups sharing similar evolutionary paths. Each of these groups represents a key kinematic element of the localisation of the fault within the modelled multilayer. For simplicity the groups are referred to in geometric terms relative to the eventual through-going fault and depending on whether they occur within strong or weak layers. They are each described in the general order in which they develop: (i) antithetic shear zones—weak layers, (ii) synthetic faults—strong layers, (iii) synthetic faults—weak layers, (iv) hanging wall splays—strong layers; whilst structures (i) and (iv) represent accommodation features associated with fault displacement, the synthetic faults ((ii) and (iii)) eventually become the through-going fault. Though the emphasis is on describing the basic deformation paths for each element, we also highlight the coupling and inter-relationships between them. Each locality in Fig. 8 is labelled A through to H according to the layer in which it occurs and individual strain

and stress paths for each of these locations are shown in Figs. 8, 9 and 10.

(i) *Antithetic shear zones—weak layers*: The two locations (D2 and F2) straddling antithetic shear zones in weak layers show similar strain/stress paths, though the zone closer to the base of the model and the future main fault (F2) shows, as expected, the larger volumetric strain and finite strain. These zones are dilational (Fig. 9b) with generally counter-clockwise (CCW) shearing (positive rotation in Figs. 8 and 9d), a dominant pure shear component (Fig. 8) and link downwards into eventual Mode I fractures, which form the main fault within the strong layers (Fig. 6). Their formation is evidently related to monoclinal folding of the intervening strong layers because they link the eventual Mode I fractures arising from outer arc folding of underlying strong layers with the complementary monoclinal hinge on the base of overlying strong layers (Fig. 7). After the first throw increment (1 cm) the weak material at both locations is in its critical stress state (Fig. 10b) and thereafter shows an almost linear increase in volumetric strain with throw (Fig. 9b). The continued growth of these antithetic shears suggests that flexuring within the hanging wall of the eventual main fault continues beyond the formation of Mode I fractures within the strong layers (Fig. 7), a feature which is ascribed to the irregularity of the trace of the eventual through-going main fault (see below). A temporary levelling off of volumetric strain at one location (D2, Fig. 9b) is attributed to the short-term cessation of extension across the Mode I fracture in the second lowest strong layer (location E1).

(ii) *Synthetic faults—strong layers*: Four locations (A, C, E1 and G1; Fig. 8) straddle the trace of the main fault within the strong layers and show similar stress/strain paths, though timing differs from one location to another. Initially the deformation at each location is characterised by clockwise (CW) rotation (negative values in Fig. 9c) accompanied by an approximately linear increase in volumetric strain (Fig. 9a) and a progressive increase in σ_I and decrease in σ_{III} (Fig. 10a). These deformations are consistent with monoclinal folding prior to fault localisation (Fig. 7). Tensile failure, i.e. Mode I fracture, of each strong layer is marked by a rapid increase in the local volumetric strain (Fig. 9a), a slight increase in rate of rotation (Fig. 9c) and, generally, by a corresponding stress release (increase in σ_{III}; Fig. 10a). The rapid volumetric strain changes and associated Mode I fracture formation do not, however, migrate progressively up the model with time. From the base of the model Mode I fracturing starts in the strong layers at 3 cm throw (G1), ca. 4.5 cm (E1), 8 cm (C) and 7 cm (A), respectively. After Mode I fracturing, most locations are characterised by simple extension (Fig. 8) with increasing dilational CW shear (Fig. 9a and c), arising from
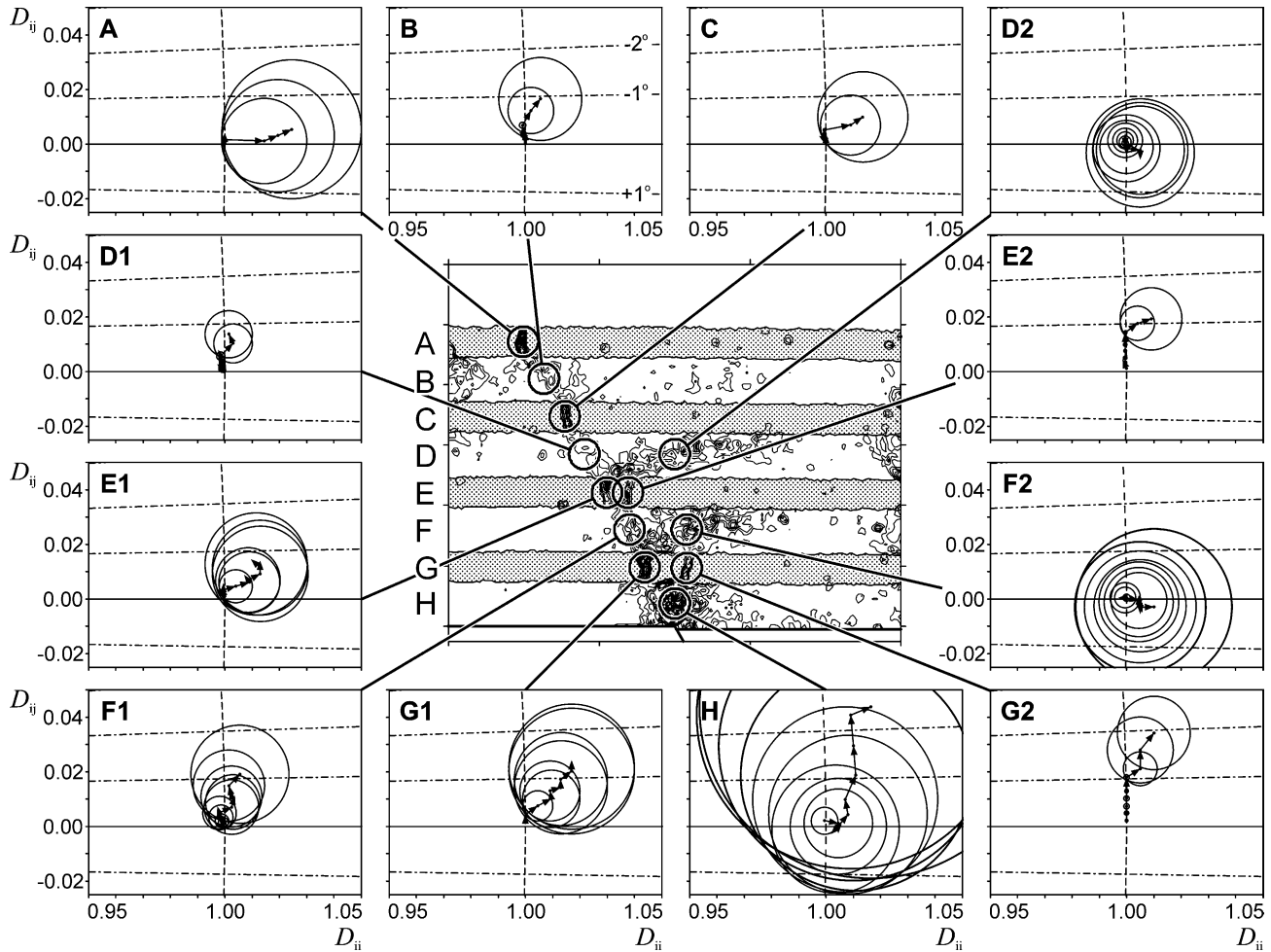
Fig. 8. Strain paths at selected locations (circled regions labelled A–H) in the multilayer model. The central diagram is of the multilayer model at a finite throw of 10 cm, which is contoured for maximum finite shear strain (contour interval is 0.01). Individual beds within the multilayer are labelled A–H. Mohr circles for finite strain at 1 cm throw increments are illustrated; arrows connect centres of successive Mohr circles. The dashed vertical arc in each Mohr diagram is part of a unit circle with its centre located at the origin. The centres of Mohr circles for rigid body rotation plot on this arc. The dash–dot lines are lines intersecting the origin with slopes in 1° intervals (labelled in B). These guidelines can give quick insights into rotations (e.g. 1° CW rigid body rotation prior to formation of pull-apart as in diagram G2). See text and Appendix A for further explanation.

pull-apart formation. A temporary cessation of displacement on the second lowest layer (at E1) is marked by a gradual increase in CW rotation (Fig. 9c) and a decrease in both σ_I and σ_{III} (Fig. 10a), with approximately constant volumetric strain (Fig. 9a). This is due to the formation of a Mode I fracture in the hanging wall of the main fault, which is active in the last two throw increments shown (see hanging wall splay—strong layer, location E2).

(iii) *Synthetic faults—weak layers*: Four locations (B, D1, F1 and H) straddle what is to become the main fault within the weak layers. One of these (location H) reaches an advanced stage very early because it is adjacent to the pre-defined fault and therefore attains high strains at low throws, immediately reaching the critical stress state of the weak material (Fig. 10b) and thereafter showing approximately linear increases in volumetric strain with throw (Fig. 9b). The rotational component at this location shows a dramatic increase after a throw of 4 cm (Fig. 9d), which coincides with

the formation of the first Mode I fracture (location G1). In contrast, the other locations (B, D1 and F1) are characterised by early stage CW rotations (Fig. 9d) with variable degrees of compaction (Fig. 9b), which are usually accompanied by increases in σ_I and little change in σ_{III} (Fig. 10b). Later stage decreases in both σ_I and σ_{III} (Fig. 10b), together with increases in volumetric strain (Fig. 9b), are associated with dilational CW shearing with a dominant simple shear component (Fig. 8). Rotation associated with monoclinal flexure occurs in each weak layer from the onset but increases abruptly at a throw of 8 cm (Fig. 9d) when the final strong layer (C) is broken and elevated shear strains occur along the entire fault trace (Fig. 6). This late stage deformation reflects fault linkage and the relatively shallow dip of the linking faults within the weak layers. At this stage the weak material is in a critical stress state (Fig. 10b) and thereafter shows an approximately linear increase in volumetric strain with throw (Fig. 9b). Again the overstep generation is not
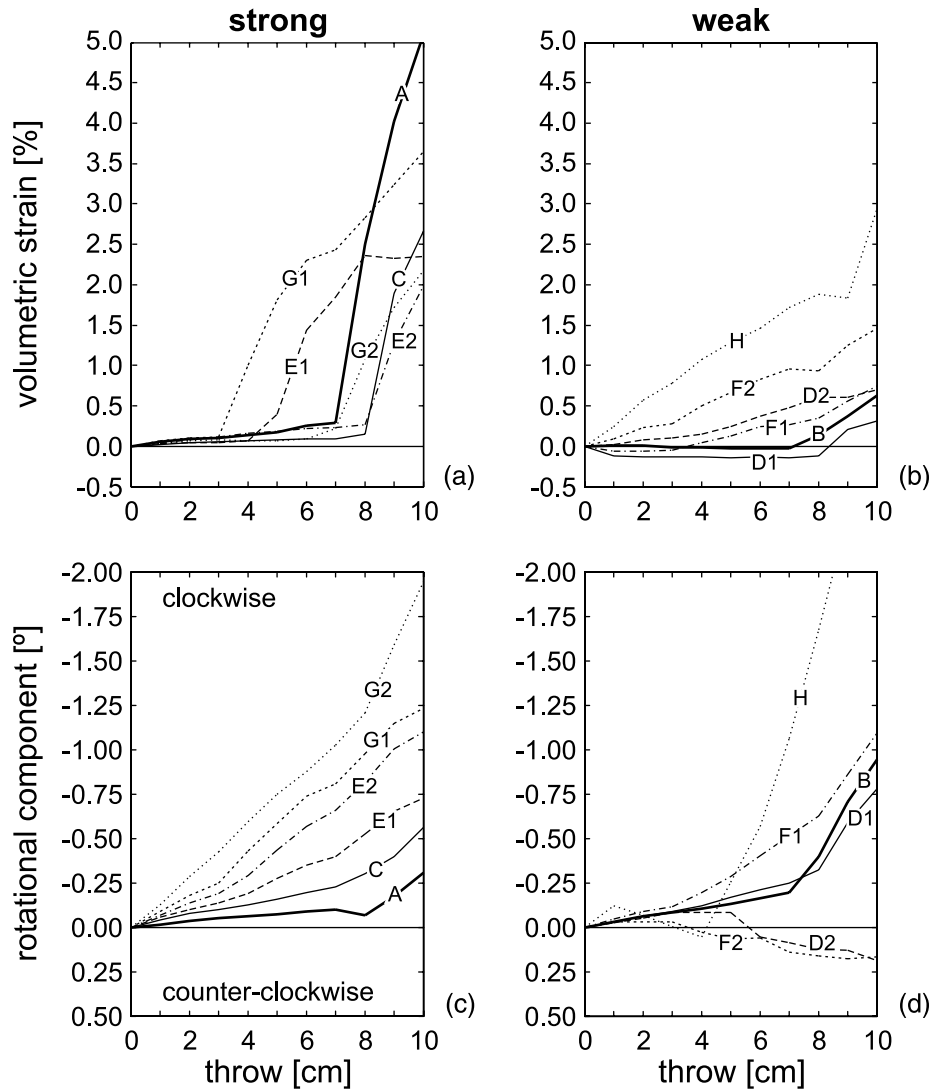
Fig. 9. Graphs of volumetric strain ((a) and (b)) and the rotational component of deformation ((c) and (d)) vs. throw for the locations labelled in Fig. 8.

progressive with linkages occurring at ca. 4 cm throw in the lower part of the model (at F1), at ca. 8 cm towards the top of the model (at B) and at ca. 10 cm towards the middle of the model (at D1). Though the deformation paths of each of the locations are similar, slight differences may offer some clues to the localisation process. The retarded localisation of a through-going fault at D1 is associated with the relatively high compaction (−0.14%) accommodated during the early stages of localisation at this location. It may also be that this retardation is, in turn, responsible for the relatively late localisation in the overlying strong layer (C) as well as the temporary cessation of movement on the underlying strong layer (E1). Whether these links are causal is unclear, but they suggest that the behaviour at different locations along the localising fault is strongly coupled.

(iv) *Hanging wall splays—strong layers*: These two locations (E2 and G2) straddle what are to become hanging wall splays within the strong layers. Although

the faults dip towards the main fault, their sense of shear is in sympathy with the main fault (Figs. 8 and 9c). The two locations show similar strain paths, though again the precise timing of events at each is different. Prior to Mode I failure at these locations (up to 7–8 cm throw) small linear increases in volumetric strain (up to 0.25%; Fig. 9a) are accompanied by substantial CW rotations (ca. 1°; Figs. 8 and 9c), rapid decreases in σ_{III} and slight increases in σ_I (Fig. 10a). The significant rotations again record the development of precursory monoclines within the strong layers, a feature that in outcrop studies would generally be referred to as normal drag (e.g. Barnett et al., 1987; Grasemann et al., 2005). When throws of ca. 3 cm (at G2) and 6 cm (at E2) are reached, Mode I fractures develop within the same layers (at G1 and E1, respectively; Fig. 6), along the trend of the incipient main fault, causing stress release and an increase in σ_{III} (Fig. 10a). Even after Mode I failure, varying degrees of rotation continue to occur at these locations (Figs. 7 and 9c), a feature that is
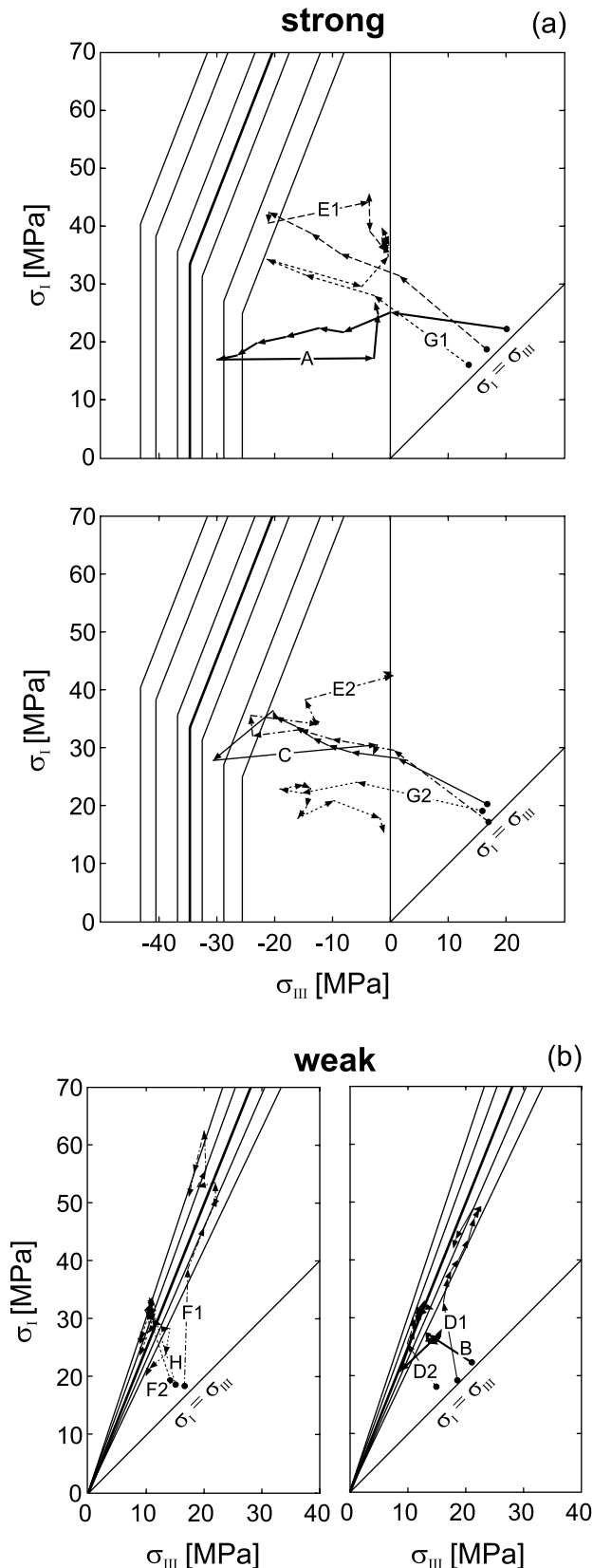
Fig. 10. Principal stress plots showing stress paths in (a) strong and (b) weak layers for the locations labelled in Fig. 8. The experimentally derived failure envelopes of Fig. 5 are also shown. For clarity, two plots, each with three stress paths, are presented for both materials. Each arrow corresponds to the change of stress in a 1 cm throw increment and dots represent the state of stress prior to faulting.'

attributed to the irregularity of the trace of the newly formed through-going fault. In both cases stress paths are looped or bouncing (Fig. 10a), indicating repeated failure of layers, before rapid increases in volumetric strain (Fig. 9a) and stress release (increase in σ_{III}) correspond to the formation of Mode I fractures (after ca. 7 cm throw at G2, and 8 cm throw at E2).

In the above discussion we considered only the local stress/strain response within the model. A proxy for the global stress/strain response of the strong layers can be obtained by tracing the strain energy stored in the bonds (i.e. elastic cement) and the bond breakage events. The average strain energy stored in each bond and the total number of broken bonds vs. throw are plotted in Fig. 11a. An initial non-linear increase in strain energy is followed by a slight drop in energy due to failure (and thus removal of bonds) of the lowest layer (G). This drop in energy is accompanied by an increase in the number of broken bonds (Fig. 11a). After the first failure, both the strain energy and number of broken bonds increase gradually until the next layer (E) fails. The failure of layers A and C show similar patterns. The drop in strain energy increases with increasing throw and no increase in strain energy is observed after the last strong layer failed (C) and a continuous fault has been established. Following localisation, the strain energy progressively decreases, stabilizing at a value equal to about half the peak value at a throw of 0.5 m (not shown).

The stress/strain paths and the strain energy/number of broken bonds described above are consistent with conceptual models of fault growth in layered sequences. Fault growth can be summarised as a three-stage process (Fig. 11b):

1. *Monoclinal flexure*: Folding is accommodated in the strong layers by elastic bending prior to failure but by flow in the weak layers, which cannot sustain bending moments. Extension and folding leads to horizontal tensile stresses within the strong layers.
2. *Failure of strong layers*: Fault segments in the strong layers develop within the precursor monocline. The layers fail in tension and Mode I fractures form. Failure of the strong layers leads to release of tensile stress (increase in σ_{III}) and a rapid increase in volumetric strain. After the first increment of failure, which is pure Mode I, the fractures develop a shear component due to the formation of pull-aparts within the strong layers. Despite the formation of fractures in the strong layers, much of the offset is still accommodated by monoclinal folding to provide a zone of fault-related normal drag.
3. *Formation of through-going fault*: After failure of all strong layers a through-going fault develops with localisation of strain in the weak layers, at a throw of ca. 0.1 m. Segment linkage leads to a staircase-geometry, with steeply dipping fault segments in the strong layers and relatively shallow dipping faults in the weak layers. With the formation of a through-going fault, normal drag becomes progressively less significant with increasing throw (beyond the 10 cm throw shown in Fig. 6) so that discontinuous shear
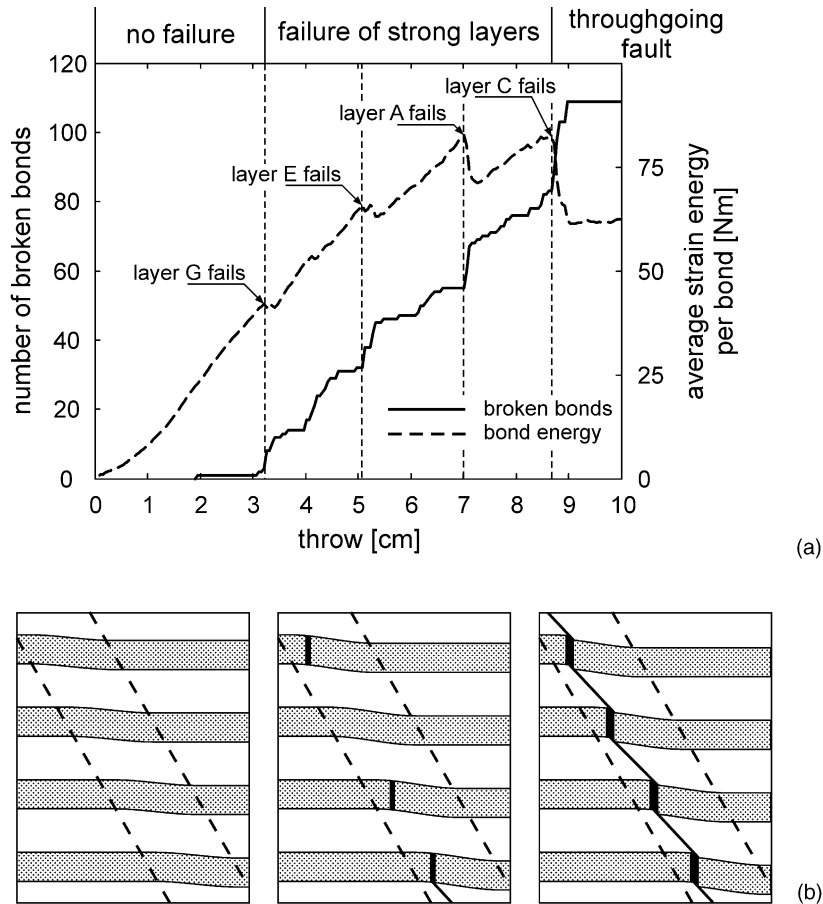
Fig. 11. Three-stage development of fault growth in a multilayer sequence as illustrated by (a) plot of number of broken bonds and average strain energy per bond vs. throw recorded in the model shown in Fig. 6 and (b) schematic representation of stages in development of the same model. The data in (a) were obtained from the model by tracking each bond breakage event and the strain energy stored in the bonds. The onset of failure of each strong layer is labelled and marked with vertical dashed lines. In (b) monoclinal flexuring is exaggerated but details of related ductile deformation are not shown. The precursory zone of faulting (bounded by the two dashed lines) is idealized as a planar feature, whereas the modelled zone broadens upwards due to the predefined nature of the fault at the base of the model (larger scale models, not presented here, indicate that a planar zone is most appropriate).'

displacement accounts for up to 60 and 85% of the total offset at throws of 0.5 and 1 m, respectively.

It is important to emphasize that only one model is analysed in detail in this study. Different model realisations, with different particle and bond spatial distributions (but identical microproperty statistical distributions) exhibit variable fault geometries due to differences in the locations of stress concentrations causing fracture nucleation. Although the exact locations of fractures and the magnitude and sense of stepping across weak layers varies between realisations, the overall fault dip and the relative timing and mode of failure (strong layers first as Mode I fractures) is not affected by varying particle and bond spatial distributions.

4. Implications for the 3D geometry of faults in multilayer sequences

The ideal conceptual image of a normal fault is that of a continuous surface entirely contained within a volume of rock and bounded by an elliptical tip-line (Watterson, 1986; Fig. 3b); more irregular tip-lines are attributed to the interaction with a

free surface or other faults (Nicol et al., 1996). For the ideal fault, displacement varies continuously over the fault surface, with contours of displacement concentric about a central maximum. Relative to this simple model, our numerical model is best suited to modelling the displacement accumulation along a vertical chord from the maximum displacement to the upper tip line. For normal faults this chord is characterised by displacement parallel propagation, with no out-of-plane or lateral propagation (Fig. 3b). Although our modelling demonstrates that, at least in its early stages, the localisation of individual faults is, perhaps not surprisingly, more complex than simple models suggest, the general upward progression of deformation away from the maximum displacement does adhere to that of the simple model. This suggestion is developed further by combining interpretations, using both finite (not shown) and incremental maximum shear strain contour diagrams (Fig. 6), of the cross-sections for different throw values of our DEM model, to produce a fence diagram of the fault traces. The fault tip-points on this fence diagram are joined to form continuous fault tip-lines outlining a series of fault segments (Fig. 12) which together represent a fault with a maximum displacement of 10 cm at one end and zero displacement on the other. Because the 3D fault plane shown in

Fig. 12 is based on 2D modelling, it does not take account of out-of-plane, or lateral, propagation effects, which are likely to increase the complexities associated with fault zone localisation. Nevertheless, the diagram illustrates several interesting features. First, the degree of segmentation decreases with increasing displacement until the segmented array is eventually replaced by a continuous fault. Second, despite the segmented nature of the fault, its overall shape approximates to one quadrant of an elliptical fault surface; the retarded localisation within layer C is responsible for the most significant departure from an approximately elliptical form. Third, displacement transfer across contractional steps is possible even when segmented arrays are underlapping, i.e. the structure between beds E and G at a throw of 4–8 cm. Finally, despite the complex nature of the fault on this scale of observation, the fault segments form a coherent array which, when considered together, resemble a simple single fault. In detail, of course, the segmented fault array shows a tip line that is more advanced in the strong layers (labelled A, C, E and G) than in the weak ones, a feature which suggests that within multilayer sequences tip-lines will be fringed. It also shows that linkage of faults in layers C and E via a shallow dipping fault in the intervening weak layer produces a branch point where the segmented array gives way laterally to a continuous fault. Most of all, this geometry emphasizes the fact that the linkage of initially vertically segmented faults does not imply that the faults grew independently, a feature that is consistent with earlier models for segmented fault arrays (Childs et al., 1995, 1996; see also the coherent growth model of Walsh et al. (2003)).

Our numerical model therefore provides a basis for extending the simple conceptual diagrams of Fig. 2 into 3D. Fig. 13 shows that a continuous fault with nearly constant displacements in cross-sectional view can give way laterally to a fringed tip-line in which fault segments within strong layers are more advanced than those within weak layers. For simplicity the block diagram in Fig. 13 considers only segmentation arising from lateral propagation. In reality segmentation will be preserved over an entire fault surface if displacements are not high enough to link between strong layers. An increase in displacement, whether or not it is accompanied by fault propagation, will lead to the progressive replacement of the segmented array by a continuous fault. Even where the fault is segmented we should expect displacements to vary systematically over the fault surface. However, when account is taken of both the discontinuous displacements on the fault and the continuous displacements accommodated by fault-related ductile deformations adjacent to the fault, displacement variations are reduced. In proportional terms, ductile deformation is likely to be more significant early in the localisation process, when fault segments remain unlinked. Continuity of displacement and related strains reflects the underlying fact that segments within an initially segmented array form a geometrically and kinematically coherent system, in which neither the displacements nor the locations of segments are incidental (coherent growth model; Walsh et al., 2003; see also Childs et al., 1995).

5. Discussion

The discrete element method (DEM), as implemented in PFC-2D, has been used to model the growth of a normal fault in a brittle/ductile multilayer. The principal advantage of the DEM compared with continuum methods (finite element, finite difference and boundary element methods) is that discrete fractures and faults with a large finite displacement can be more effectively modelled; advances in combined approaches (DEM–FEM) may, however, provide an even better basis for future fault and fracture modelling. The main limitations in the modelling approach in this study are that the model materials are strain-rate independent and that fluids and their effects (e.g. over-pressuring, precipitation of minerals) are neglected. Despite these limitations, the modelling is capable of reproducing many of the characteristic features of natural faults, providing a mechanical rationale for their geometry and growth. In particular, it provides a basis for investigating whether normal faults in layered sequences localise first in the strong layers or the weak layers (Ferrill and Morris, 2003), a question that cannot be addressed using conventional mechanical analyses such as Mohr stress diagrams (Mandl, 2000).

The DEM models presented in this article incorporate properly calibrated model materials that reproduce the behaviour of natural rocks. The brittle/ductile multilayer sequence comprises strong layers, which are brittle at low–intermediate confining pressures and have elastic properties and strengths similar to those of strong sedimentary rocks, interbedded with weak layers, which are cohesionless, frictional-plastic and cannot sustain bending moments. Faulting in such a layered sequence leads to an increase in layer parallel tensile stress (decrease in σ_{III}) and an increase in volumetric strain in the strong layers until the material fails in tension (Mode I). Diffuse zones of pure shear dominated deformation (squeeze flow) in the weak layers accommodate small amplitude precursor folding of the strong layers prior to failure. Deformation in these zones has a small rotational component that is antithetic with respect to the main fault and is in that respect similar to the antithetic 'damage zones' at the tip of faults in homogeneous, non-layered rocks described by Kim et al. (2003). Although both types of antithetic faults form within a zone of distributed shear, the geometries of antithetic faults in our DEM models are strongly affected by layering, since they link the hinges of a fault related monocline. In our model, Mode I fractures within the strong layers form an initial vertically segmented fault array that is later linked via shallow dipping faults in the weak layers. The model results provide a mechanical basis for fault refraction arising from different modes of faulting within different layers, with tensile failure in the strong layers and shear failure in the weak layers. At overburden pressures greater than that applied here (> ca. 100 MPa) the strong layers in this model fail in shear rather than in tension, but even in these circumstances faults tend to initiate first within the strong layers and the fault zone is an initially vertically segmented array. As in the low effective stress model the fault dips within the strong layers are

Fig. 12. 3D fault plane constructed from interpreted fault traces from the PFC-2D model shown in Fig. 6 assuming the temporal fault zone evolution is equivalent to spatial variation in fault zone structure with increasing displacement. Labelled layers (A, C, E and G) are strong layers. To construct this diagram, the lateral displacement gradient was taken as 1:150, i.e. 1.5 m distance along strike between successive sections in Fig. 6. The fault is typically more advanced in the strong layers; the advancement within layer C is approximated, since no section is available at a throw of 8.5 cm.

controlled by the failure mode, whereas the fault dips within the weak layers are mainly controlled by segment linkage.

The model suggests also that abandoned fault tips or splays are not essential features of an initially vertically segmented array. Fault segments that underlap and do not generate abandoned tips and splays when they link can form coherent arrays and show complementary displacement transfer, provided that the intervening volume can accommodate ductile strain. The model highlights the fact that the initially vertically segmented fault array is geometrically and kinematically coherent (Walsh and Watterson, 1991; Walsh et al., 2003) and that the fault segments do not grow independently in individual layers (Contra Benedicto et al., 2003) but could link laterally into a continuous fault (fig. 9 in Childs et al., 1996).

The model also demonstrates that initial Mode I fracturing is not necessarily an indicator of high pore pressure. Fluid pressure only increases the depth of possible tensile failure since it decreases the effective stress. Fault refraction at low effective stress is not 'due to high pore pressure' but due to different types of failure (extension vs. shear) in the different lithologies (Peacock and Sanderson, 1992). The suggestion that fault segmentation is a product of fault propagation (e.g. Jackson, 1987; Mandl, 1987; Cox and Scholz, 1988; Peacock and Zhang, 1993; Childs et al., 1996; Marchal et al., 2003; Walsh et al., 2003)

Fig. 13. Conceptual growth model for normal faults cutting limestone layers of the Buda Limestone (see Fig. 2). The block diagram is located at a lateral fault tip (Fig. 3b). For simplicity the fault is shown with no vertical displacement gradient. The block diagram was constructed using cross-sections shown in Fig. 2a and b.

is supported by DEM modelling, though the importance of mechanical layering in controlling segmentation cannot be overstated.

6. Conclusions

The DEM, as implemented in PFC-2D, has been used for modelling the growth of a normal fault within a brittle/ductile multilayer sequence. Our research suggests that the DEM is capable of modelling the failure and localisation processes of faulting, aspects that cannot be modelled adequately using conventional continuum based methods. Our modelling provides new insights into both the mechanics and kinematics of faulting at low effective stresses and suggests the following principal conclusions:

- Large dip variations, and related fault refraction, are due to different types of failure (extension vs. shear) of layers.
- Normal faults in brittle/ductile sequences localise first in strong layers as steeply dipping Mode I fractures and are later linked via shallow dipping faults in weak layers. With increasing displacement arrays of fault segments are therefore replaced by a continuous fault.
- Faults contained in multilayer sequences have fringed tip lines, where the fault is laterally more advanced in the strong layers than in the weak layers. The extent of fringing is a function of fault displacement and of the strength contrast between the layers.
- Models for the 3D segmentation of faults in sedimentary sequences must include the effects of rock properties and mechanical layering.

Appendix A. Mohr Circles for D

An extremely useful graphical representation of the position gradient tensor is the Mohr circle for **D** (e.g. Means, 1983, 1990).

Any 2D, homogeneous deformation can be written as

$$\begin{pmatrix} x_1 \\ x_2 \end{pmatrix} = \begin{pmatrix} D_{11} & D_{12} \\ D_{21} & D_{22} \end{pmatrix} \begin{pmatrix} X_1 \\ X_2 \end{pmatrix} \tag{A1a}$$

or more compactly as

$$\mathbf{x} = \mathbf{DX}, \tag{A1b}$$

where **X** and **x** are position vectors for a particle in the undeformed and deformed state, respectively, and D_{11}, D_{12}, D_{21} and D_{22} are the components of the position gradient tensor **D**, which contains information about the stretch and rotation and is referred to as the deformation tensor in this Appendix.

The components of **D** can be obtained by deforming a unit square into a parallelogram (Fig. A1a). Components D_{11} and D_{21} are determined using the x_1 and x_2 coordinates of the corner point that was located at $(1,0)$ whereas components D_{12} and D_{22} are obtained using the x_1 and x_2 coordinates of the corner point that was located at $(0,1)$ in the undeformed state.
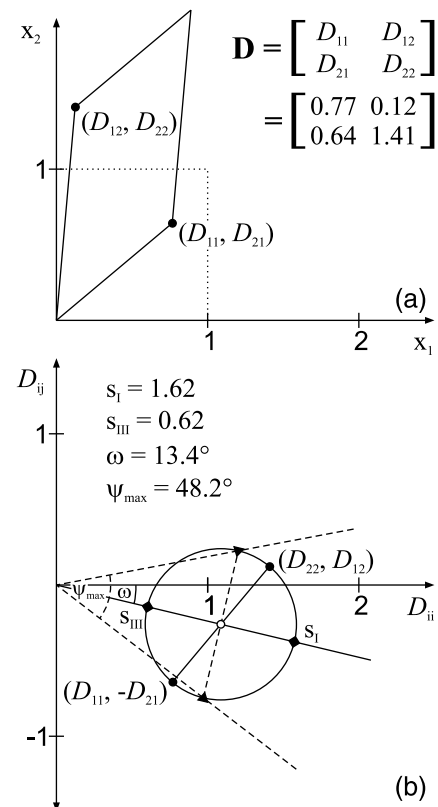

Fig. A1. Plotting and reading Mohr circles for **D**. (a) The components of the deformation tensor (D_{11} etc.) are derived from the corners of the deformed unit square as shown. The deformation tensor for this parallelogram is also given. (b) Mohr circle representation of the **D** tensor. The constructions for finding the principal stretches, s_I and s_{III}, the rotational component of deformation, ω, and the maximum angular shear strain, ψ_{max}, are illustrated. See Appendix A for further explanation.
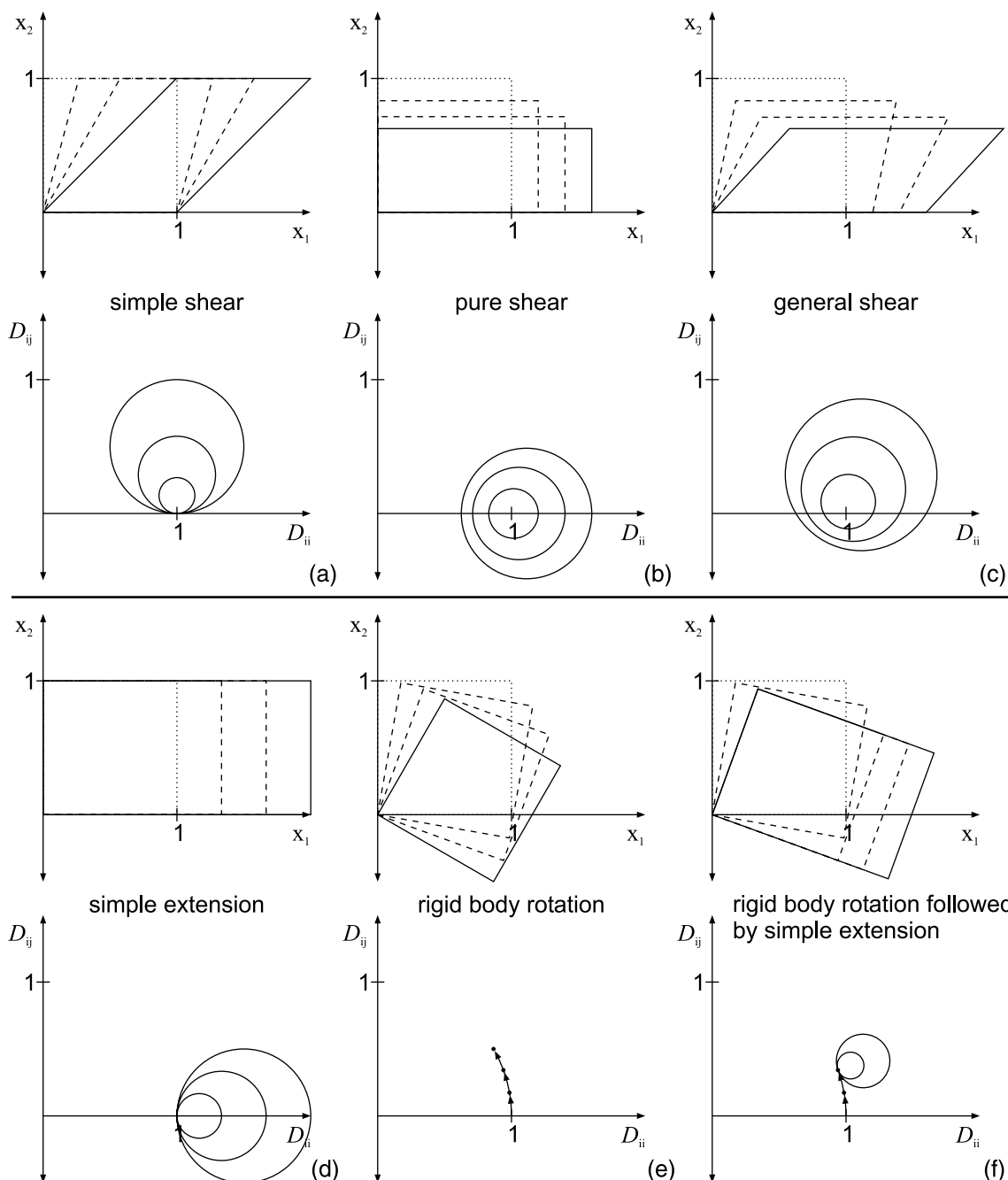
Fig. A2. Illustrations of Mohr circles for deformation, **D**, for a range of strain paths. For each labelled example the Mohr circles and the corresponding deformed unit square in Cartesian coordinates (dotted lines) are shown (the finite state of strain is shown as solid lines and intermediate stages are shown as dashed lines). Strain paths in (a)–(c) are constant volume deformation. The strain path shown in (d) is irrotational simple extension (dilation), (e) is rigid body rotation without stretching and (f) is rigid body rotation (e.g. normal drag in the context of faulting) followed by simple extension (e.g. the formation of a Mode I fracture). In (d) and (f) only one set of parallel lines exists that shows neither finite nor incremental stretch.

A Mohr circle (of the first kind; De Paor and Means, 1984) representing **D** is drawn using equally calibrated axes for the normal (D_{11}, D_{22}) and shear components (D_{12}, D_{21}). Two points are plotted at (D_{11}, $-D_{21}$) and (D_{22}, D_{12}), connected by a line and a circle is drawn about this line (Fig. A1b). The polar co-ordinates of any point on the **D** circle give the stretch and rotation of a material line.

The principal stretches, s_I and s_{III} ($s_I > s_{III}$), can be graphically obtained by intercepting the circle with a line drawn from the origin through the centre of the circle (Fig. A1b). The diameter of the Mohr circle is therefore related to the intensity of stretching, since the ellipticity of the strain ellipse is s_I/s_{III}. The volumetric strain (strictly speaking area change), which cannot be directly read off the Mohr diagram, is the product of the principal stretches minus one.

Symmetric deformation tensors ($D_{12} = D_{21}$) represent irrotational deformation and associated Mohr circles have their centre on the horizontal axis (Fig. A2b and d). Mohr

circles of this kind are often referred to as Mohr circles for stretch. Asymmetrical deformation tensors ($D_{12} \neq D_{21}$) represent rotational deformation (Figs. A1 and A2a and c). The rotational component of any strain is given by

$$\tan \omega = \frac{D_{21} - D_{12}}{D_{11} + D_{22}} \qquad (A2)$$

and can be obtained graphically by measuring the angle between a line drawn from the origin to the centre of the circle and the horizontal axis where, by definition, clockwise rotation is negative (Fig. A1b). Off-axis circles centred above the horizontal axis represent deformation with a clockwise (by convention negative) rotational component (Fig. A2a and c).

Rigid body rotation leads to circles with zero radius and centres on a unit circle in the Mohr diagram (Fig. A2e). In this study it has proven useful to plot a unit circle with its centre in the origin and lines with slopes in 1° intervals (Fig. 8). These guidelines assist in estimating the amount of rigid body rotation prior to stretching.

The maximum angular shear strain is given by

$$\tan \psi_{max} = \frac{s_I^2 - s_{III}^2}{2 s_I s_{III}} \qquad (A3)$$

and can be obtained graphically by drawing a chord through the centre of the circle perpendicular to the line that passes through the principal stretches (Fig. A1b). The intersection of the chord with the circles gives the points that represent material lines that were perpendicular to each other in the undeformed state (as usual double angles are measured in Mohr circles). This pair of lines experienced the maximum shear strain, since they are symmetrically arranged with angles of $\pm 45°$ to the principal stretches in the undeformed state (Fig. A1b).

References

Barnett, J.A.M., Mortimer, J., Rippon, J.H., Walsh, J.J., Watterson, J., 1987. Displacement geometry in the volume containing a single normal fault. Bulletin of the American Association of Petroleum Geologists 71, 925–937.

Benedicto, A., Schultz, R.A., Soliva, R., 2003. Layer thickness and the shape of faults. Geophysical Research Letters 30, 2076. doi:10.1029/2003GL018237.

Burbidge, D.R., Braun, J., 2002. Numerical models of the evolution of accretionary wedges and fold-and-thrust belts using the distinct-element method. Geophysical Journal International 148, 542–561.

Childs, C., Watterson, J., Walsh, J.J., 1995. Fault overlap zones within developing normal fault systems. Journal of the Geological Society, London 152, 535–549.

Childs, C., Nicol, A., Walsh, J.J., Watterson, J., 1996. Growth of vertically segmented normal faults. Journal of Structural Geology 18, 1389–1397.

Cox, S.J.D., Scholz, C.H., 1988. On the formation and growth of faults: an experimental study. Journal of Structural Geology 10, 413–430.

Crider, J.G., Peacock, D.C.P., 2004. Initiation of brittle faults in the upper crust: a review of field observations. Journal of Structural Geology 26, 691–707.

Cundall, P.A., Hart, R., 1992. Numerical modeling of discontinua. Engineering Computations 9, 101–113.

Cundall, P.A., Strack, O.D.L., 1979. A discrete numerical model for granular assemblies. Géotechnique 29, 47–65.

De Paor, D.G., Means, W.D., 1984. Mohr circles of the First and Second Kind and their use to represent tensor operations. Journal of Structural Geology 6, 693–701.

Eisenstadt, G., De Paor, D.G., 1987. Alternative model of thrust-fault propagation. Geology 15, 630–633.

Fakhimi, A., 2004. Application of slightly overlapped circular particles assembly in numerical simulation of rocks with high friction angles. Engineering Geology 74, 129–138.

Ferrill, D.A., Morris, A.P., 2003. Dilational normal faults. Journal of Structural Geology 25, 183–196.

Finch, E., Hardy, S., Gawthorpe, R., 2003. Discrete element modelling of contractional fault propagation folding above rigid basement fault blocks. Journal of Structural Geology 25, 515–528.

Finch, E., Hardy, S., Gawthorpe, R., 2004. Discrete-element modelling of extensional fault-propagation folding above rigid basement fault blocks. Basin Research 16, 489–506.

Grasemann, B., Martel, S., Passchier, C., 2005. Reverse and normal drag along a fault. Journal of Structural Geology 27, 999–1010.

Hazzard, J.F., Young, R.P., Maxwell, S.C., 2000. Micromechanical modeling of cracking and failure in brittle rocks. Journal of Geophysical Research 105, 16,683–16,697.

Hoek, E., Brown, E.T., 1997. Practical estimates of rock mass strength. International Journal of Rock Mechanics & Mining Science 34, 1165–1186.

Imber, J., Tuckwell, G.W., Childs, C., Walsh, J.J., Manzocchi, T., Heath, A.E., Bonson, C.G., Strand, J., 2004. Three-dimensional distinct element modelling of relay growth and breaching along normal faults. Journal of Structural Geology 26, 1897–1911.

Itasca Consulting Group, 1999. Particle Flow Code in Two Dimensions, Minneapolis, MN, USA 1999.

Jackson, P., 1987. The corrugation and bifurcation of fault surfaces by cross-slip. Journal of Structural Geology 9, 247–250.

Jaeger, J.C., Cook, N.G.W., 1976. Fundamentals of Rock Mechanics, 2nd ed Chapman & Hall, London.

Kim, Y.-S., Peacock, D.C.P., Sanderson, D.J., 2003. Mesoscale strike-slip faults and damage zones at Marsalforn, Gozo Island, Malta. Journal of Structural Geology 25, 793–812.

Mandl, G., 1987. Discontinuous fault zones. Journal of Structural Geology 9, 105–110.

Mandl, G., 2000. Faulting in Brittle Rocks. Springer, Berlin, Heidelberg, New York.

Marchal, D., Guiraud, M., Rives, T., 2003. Geometric and morphological evolution of normal fault planes and traces from 2D to 4D data. Journal of Structural Geology 25, 135–158.

McGrath, A.G., Davison, I., 1995. Damage zone geometry around fault tips. Journal of Structural Geology 17, 1011–1024.

Means, W.D., 1983. Application of the Mohr-circle construction to problems of inhomogeneous deformation. Journal of Structural Geology 5, 279–286.

Means, W.D., 1990. Kinematics, stress, deformation and material behavior. Journal of Structural Geology 12, 953–971.

Nicol, A., Watterson, J., Walsh, J.J., Childs, C., 1996. The shapes, major axis orientations and displacement patterns of fault surfaces. Journal of Structural Geology 18, 235–248.

Oda, M., Iwashita, K., 2000. Study of couple stress and shear band development in granular media based on numerical simulation analyses. International Journal of Engineering Sciences 38, 1713–1740.

O'Sullivan, C., Bray, J.D., Li, S., 2003. A new approach for calculating strain for particulate media. International Journal for Numerical and Analytical Methods in Geomechanics 27, 859–877.

Paul, B., 1961. A modification of the Coulomb–Mohr theory of fracture. Journal of Applied Mechanics 28, 259–268.

Peacock, D.C.P., Sanderson, D.J., 1992. Effects of layering and anisotropy on fault geometry. Journal of the Geological Society London 149, 793–802.

Peacock, D.C.P., Zhang, X., 1993. Field examples and numerical modelling of oversteps and bends along normal faults in cross-section. Tectonophysics 234, 147–167.

Petley, D.N., 1999. Failure envelopes of mudrocks at high confining pressures. In: Aplin, A.C., Fleet, A.J., Macquaker, J.H.S. (Eds.), Muds and Mudstones. Geological Society of London Special Publication 158, pp. 61–71.

Potyondy, D.O., Cundall, P.A., 2004. A bonded-particle model for rock. International Journal of Rock Mechanics and Mining Sciences 41, 1329–1364.

Strayer, L.M., Suppe, J., 2002. Out-of-plane motion of a thrust sheet during along-strike propagation of a thrust ramp: a distinct-element approach. Journal of Structural Geology 24, 637–650.

Tsiambaos, G., Sabatakakis, N., 2004. Considerations on strength of intact sedimentary rocks. Engineering Geology 72, 261–273.

Walsh, J.J., Watterson, J., 1991. Geometric and kinematic coherence and scale effects in normal fault systems. In: Roberts, A.M., Yielding, G., Freeman, B. (Eds.), The Geometry of Normal Faults. Geological Society of London Special Publication 56, pp. 193–203.

Walsh, J.J., Bailey, W.R., Childs, C., Nicol, A., Bonson, C.G., 2003. Formation of segmented normal faults: a 3-D perspective. Journal of Structural Geology 25, 1251–1262.

Watterson, J., 1986. Fault dimensions, displacements and growth. Pure and Applied Geophysics 124, 365–373.